Nurul Z. Noor Azman et al., Electrospun bismuth oxide/polylactic acid nanofibre mats, J. Synchrotron Rad. (2013). 20, 741–748

Characteristics of X-ray attenuation in electrospun bismuth oxide / poly-lactic acid nanofibre-mats

Nurul Z Noor Azman[ab], Salim A Siddiqui[a], Hazim J Haroosh[c], Hani M M Albetran[a], Bernt Johannessen[d], Yu Dong[e] and It M Low[a]*

[a]Department of Imaging and Applied Physics, Curtin University, GPO Box U1987, Perth, WA, 6845, Australia, [b]School of Physics, Universiti Sains Malaysia, Pulau Pinang, 11800, Malaysia, [c]Department of Chemical Engineering, Curtin University, GPO Box U1987, Perth, WA, 6845, Australia, [d]The Australian Synchrotron, Melbourne, VIC, 3168, Australia, and [e]Department of Mechanical Engineering, Curtin University, GPO Box U1987, Perth, WA, 6845, Australia

Correspondence email: j.low@curtin.edu.au

Keywords: Electrospun nano-Bi_2O_3/PLA nanofibre mat, electrospun micro-Bi_2O_3/PLA nanofibre mat, nano-Bi_2O_3/PLA thin films, micro-Bi_2O_3/PLA thin films, X-ray attenuation, porosity.

Synopsis

Investigation of the x-ray attenuation by electrospun nano(n)- and micro(m)-Bi_2O_3/poly lactic acid (PLA) nanofibre mats with different Bi_2O_3 loadings using mammography and XAS unit.

Abstract

The characteristics of the X-ray attenuation in electrospun nano(n)- and micro(m)-Bi_2O_3/poly lactic acid (PLA) nanofibre mats with different Bi_2O_3 loadings were compared as a function of energy using mammography (*i.e.* tube voltages of 22-49 kV) and X-ray absorption spectroscopy (XAS) (7-20 keV). Results indicate that X-ray attenuations by electrospun n-Bi_2O_3/PLA nanofibre mats are distinctly higher than those of m-Bi_2O_3/PLA nanofibre mats at all energies investigated. In addition, with increasing the filler loading (n-Bi_2O_3 or m-Bi_2O_3), the porosity of the nanofibre mats decreased thus increasing the X-ray attenuation except for the sample containing 38 wt.% of Bi_2O_3 (the highest loading in the present study). The latter showed higher porosity with some beads formed, thus resulting in a sudden decrease in the X-ray attenuation.

1. Introduction

Nanoparticles, *i.e.* nanometric sized particles, have attracted much attention amongst researchers in different fields of physics, chemistry, material science, medicine, and biology, because of their unique and often superior electronic, magnetic, optical, mechanical, physical and chemical properties (Patra et al., 2010, Huang & El-Sayed, 2010, Granmayeh Rad et al., 2011, Sahare et al., 2007, M.G, 2008, Haiwen et al., 2006, Popov, 2009). For example, in the medical field, nanoparticles have been widely used in diagnosis, tissue engineering and also as drug delivery devices (Storrie & Mooney, 2006). Gold nanoparticles are one of the most useful nanoparticles in industry and medicine (Granmayeh Rad et al., 2011). For instance in the medical field, gold nanoparticles show significant improvement in the treatment of cancers by enhancing the sensitivity of radiation from a radiotherapy unit with minimal adverse effects on surrounding normal tissues (Patra et al., 2010, Huang & El-Sayed, 2010).

Additionally, this size-effect has also become one of the virtues in designing materials for shielding of ionizing radiations. Some X-ray technologists believe that this effect will improve the X-ray attenuation ability of the composite since nano-sized fillers are able to be dispersed more uniformly within the matrix with less agglomerations as compared to micro-sized fillers consequently affect the density and composition that modify the total attenuation coefficient of the composite (Botelho et al., 2011, El Haber & Froyer, 2008). The latest work done by Buyuk et al. (2012) proved that decreasing the titanium diboride particle size in the titanium diboride reinforced boron carbide-silicon carbide composites results in a higher linear attenuation coefficient for the energy of 0.662 MeV emitted by a Cs-137 gamma source (Buyuk et al., 2012). In a complementary finding, a recent study by Botelho et al. (Botelho et al., 2011) showed that nanostructured copper oxide (CuO) is more effective in attenuating lower X-ray beam energies of tube voltages (26 and 30kV), whilst no significant variation in the X-ray attenuation at higher energies of tube voltages (60 and 102 kV) were observed. Kunzel et al. (Künzel & Okuno, 2012) also provided similar results, showing that the X-ray beam attenuation is greater for a nanostructured CuO compound compared to the microstructured counterpart for low energies of tube voltages (25 and 30 kV) for a wide range of CuO concentrations incorporated into polymeric resins.

Electrospinning is a well-established polymer processing technique which has been proven to be a flexible and effective method for fabricating multilayers of microscale (>1 μm) to the nanoscale (<1000 nm) fibres from different types of polymers used in a wide range of applications such as in drug delivery, tissue engineering and protective clothing (Faccini et al., 2012, Molamma et al., 2008, Sill & von Recum, 2008, Russo & Lamberti, 2011, Huang et al., 2012, Haroosh et al., 2012, Yiin-Kuen & Li-Chih, 2013, Rajeswari et al., 2012, Hu et al., 2010, Yu et al., 2009). This technique provides many benefits to industry with perhaps the most important one being its versatility and simplicity, which means it is a very time efficient way to fabricate a variety of continuous nanofibrous structures. It is advantageous to use the nanofibre webs in a layered structure together with a suited substrate material such that the final product offers sufficient strength and durability. Besides, the nanofibre layers should be flexible and also have a good adherence to the substrates without easily being broken or delaminated (Faccini et al., 2012, Lee & Obendorf, 2007, Brettmann et al., 2012). Moreover, some researchers have shown that electrospinning can improve the dispersion of nanoparticles within the polymer matrix thereby improving the properties of nanocomposites (Demir et al., 2004, Shanshan et al., 2010).

Polylactic acid (PLA) fibres are polymeric in nature and provide the inherent performance of fibres together with the positive environmental advantages of being renewable and recyclable. In addition, production of PLA emits less CO_2 compared with other petroleum-based fibres. Disposal of PLA not only fits within the existing disposal systems but also includes the additional option of composting (Farrington et al., 2005). Meanwhile, Bi_2O_3 is non-hazardous and is also a relatively environmentally friendly compound that is used as a substitute for toxic lead oxide which is widely used in the production of lead glass. For example, Bi_2O_3-based glasses have gained fascination among glass researchers because of their non-linear optical properties which are important for the development of optical information processing technology (An et al., 2006). Thus, they have played an important role in the replacement of lead glass by radiation shielding glass (Chanthima et al., 2011).

In the present study, given the simplicity of the electrospinning technique, it is investigated whether electrospinning can also be used to produce nanofibre mats for the efficient shielding of ionizing

radiations. In a recent work on WO_3-filled epoxy composites (Noor Azman et al., 2013), we investigated the X-ray attenuation effect of nano- and micro-sized fillers in epoxy composites over an X-ray tube voltage range of 22-127 kV. Our results showed that nano-sized WO_3 was more effective than its micro-sized counterpart in attenuation of low X-ray tube voltages (22-35 kV). This is explained by the domination of photoelectric interaction at low photon energy and also the number of W particles/gram in the nano-sized WO_3-epoxy composite being greater than that for the micro-sized WO_3-epoxy composite. The size effect was not apparent at the higher X-ray tube voltage range of 40-120 kV. Hence, the objective of our present study is to synthesize new radiation shielding materials using the electrospinning technique with the preparation of well-dispersed Bi_2O_3 of different particle sizes in PLA fibre mats. The effectiveness of electrospun nano-Bi_2O_3/PLA nanofibre mats in radiation protection during diagnostic imaging using low X-ray energies is also reported, with the ultimate goal of offering a new approach to radiation protection, based on nanotechnology and electrospinning technique to produce composites that are environmentally friendly.

2. Experimental Procedure

2.1. Materials

Bismuth (III) oxide (Bi_2O_3) particles of sizes 90-210 nm and 10 μm were used as filler for synthesizing electrospun Bi_2O_3/poly lactic acid (PLA) nanofibre mats and Bi_2O_3/PLA thin films. Bi_2O_3, chloroform and methanol were obtained from Sigma-Aldrich. Meanwhile, PLA (3051D) pellets,with the molecular weight Mn = 93,500 g mol and glass transition temperature Tg = 65.50 ^oC were supplied by NatureWorks USA.

2.2. Sample preparation

Electrospinning was carried out using 9% wt/v PLA solution by mixing with 8 mL of chloroform and 2 mL methanol as the solvents. The micro(m)-Bi_2O_3 and nano(n)-Bi_2O_3 suspension was added at 24 - 38 wt.% to the polymer solution and was homogenized for 45 min under ultrasonication. For the electrospinning process, the solutions were transferred to a 10-mL syringe pump with 25-G needles.

The flow rate of the polymer solution was 1 mL/h, and the applied positive voltage was ~19 kV. The distance between the needle tip and the target was set at 12 cm. The resulting nanofibre mats were collected on a flat aluminum foil over ~ 2 hours to achieve an acceptable thickness for X-ray attenuation experiments. The nanofibre mats were removed from the aluminium foil and cut to a dimension of 2.0 × 1.5 cm^2 or was folded together before cutting so that the nanofibre mat has an acceptable thickness for a reliable X-ray attenuation experiment. Three sets of the same nanofibre mats were prepared. The list of prepared electrospun Bi_2O_3/PLA nanofibre mats with different weight percentages of Bi_2O_3 are shown in Table 1.

The solution casting method was performed to prepare Bi_2O_3/PLA thin films for verifying the X-ray attenuation results obtained for electrospun Bi_2O_3/PLA fibre mats. In this method, PLA was mixed with the chloroform without methanol (since methanol was only used in the electrospinning process to increase the conduction of the solution and will totally evaporate during the process) of the same amount as in the electrospinning process and was homogenized for 45 min under ultrasonication. Then, the solution was poured into a beaker of 5 cm diameter and left in the fume cupboard for 24 hours to dry. Next, the thin film was removed from the beaker and three sets of the same thin film were cut to pieces of 2.0 × 1.5 cm^2 for X-ray attenuation experiments. The list of prepared Bi_2O_3/PLA thin films with different weight percentages of Bi_2O_3 are the same as shown in Table 1.

2.3. Measurements of sample thickness and porosity

Since it is inherently difficult to produce all the electrospun fibre mats to have a uniform thickness, which is an important factor in X-ray attenuation comparison, the nanofibre mat thickness for each sample was measured by determining their weight and surface area. The average thickness (t_{ave}) of the mats was then determined from Equation (1) where m is the mass, A is the surface area; and ρ is the apparent density of the electrospun mats.

$$t_{ave} = \frac{m}{A\rho} \qquad (1)$$

The apparent density (ρ) was accurately measured using the density bottle method (ASTM D854) and an average of three measurements were taken for each mat. The porosity of the mats was calculated using Equation (2). A calibrated single pan electrical balance and distilled water were used for this purpose.

$$Porosity\ (\%) = \left(1 - \frac{\rho}{\rho_{theory}}\right) \qquad (2)$$

Where ρ_{theory} is the bulk density of the Bi_2O_3/PLA composite.

Meanwhile, for the thin films the average thickness t_{ave} was measured using a vernier caliper. The apparent density (ρ) of the thin films was calculated using Equation (1) with m and A being the film mass and surface area, respectively.

2.4. Measurement of X-ray attenuation

Two separate instruments were used to characterize the X-ray attenuation of the samples. The first involved the use of the X-ray absorption Spectroscopy (XAS) beamline at the Australian Synchrotron. Experiments were carried out in the energy range of 7 – 20 keV using a Si (311) monochromator and a beam size on the sample of about 0.25 by 0.25 mm^2 and a photon flux of about 10^9 ph/s. Transmission data were collected using ionization chambers before and after the sample in placed. For each sample 20 readings were recorded at each energy. To normalize the data readings were also recorded for beam going through the air.

The second instrument used was a mammography unit (brand: Siemens AG, model: 2403951-4 G.E Health Care) at Royal Perth Hospital, Western Australia. For the work with this mammography unit, the exposure was set at 10 mAs to obtain meaningful readings for the DIADOS diagnostic detector connected to the diagnostic dosimeter (PTW-Freiburg, Germany) and the range 22 – 49 kV of X-ray tube voltage was selected. The dosimeter is a universal dosimeter for measuring simultaneous dose and dose rate for radiography, fluoroscopy, mammography, dental X-ray and CT with a sensitivity of 0.01 microRoentgen (μR). Three different anode/filter combinations (Table 2) were used for filtering

the X-ray beam produced by the chosen X-ray tube voltages used for the mammography machine, since the combination was controlled by the machine itself. The X-ray beams generated by these anode/filter combinations composed mainly of the characteristic X-ray energies of molybdenum (17.5 keV and 19.6 keV) or rhodium (20.2 keV and 22.7 keV). For each sample, the measurements were performed three times. The detector was placed 86 cm under the X-ray tube since this is the maximum distance that can be adjusted for the mammography unit, and the X-ray beam was well collimated to the size of the sample size to minimize the scattered X-ray produced by the sample.

The incident intensity I_o and transmitted intensity I (normalised to the case without a sample) were measured and the X-ray transmission ($T= I/I_o$) is related to the linear attenuation coefficient (μ) through Equation (3):

$$T = \left(\frac{I}{I_o}\right) = e^{-\mu t_{ave}} \quad (3)$$

Hence, Equation (3) can be re-write as Equation (4):

$$\mu = \frac{-\ln T}{t_{ave}} \quad (4)$$

where the X-ray transmission T is determined by μ which is the total linear attenuation coefficients of a PLA nanofibre mat or PLA thin film with Bi_2O_3 particles and pores expressed as $(\mu_{mat\ or\ film})x + (\mu_{Bi2O3})y + (\mu_{pores})z$, where x+y+z=1 is the weighted fraction contributions of the individual components.

A graph of the X-ray linear attenuation coefficient (μ) as a function of X-ray energy was plotted for each sample.

2.5. Scanning electron microscopy (SEM)

The depth profile of the samples was examined using Zeiss Evo 40XVP scanning electron microscope at a voltage of 15 kV with the working distance between 8.0 – 9.0 mm. Both secondary electrons (SE) and backscattered electron (BSE) techniques coupled with an energy dispersive X-ray spectroscopy (EDS) probe were performed after standard coating with platinum to minimize charging to show the

different of the image due to the different atomic number of PLA and Bi. A pure electrospun PLA nanofibre mat was also examined as a benchmark.

3. Results and discussion

3.1. Thickness and porosity measurement

The average thickness t_{ave} for all the electrospun Bi_2O_3/PLA nanofibre mats measured are in the range of 0.006 -0.014 cm while for Bi_2O_3/PLA thin films are in the range of 0.04 – 0.08 cm respectively. All of these t_{ave} measurements will be used in Equation (4) to calculate the value of μ for each sample.

From Table 3, the apparent density ρ of each thin film (the last two columns to the right of the table) of the same filler (Bi_2O_3) category increased by the increment of filler content in the PLA solution. The density found in thin films illustrate that m-Bi_2O_3/PLA thin films have lower density compared to n-Bi_2O_3/PLA thin films though neither are significantly different to their theoretical value. However, the apparent density of the electrospun Bi_2O_3/PLA nanofibre mats underestimated the theoretical values due to the nanofibres being highly porous, randomly oriented and aligned. As can be seen, the density of the electrospun Bi_2O_3/PLA nanofibre mat increased with the filler loading except for the electrospun Bi_2O_3/PLA nanofibre mat of 38 wt.% Bi_2O_3 loading; there is a sudden decrease in the density due to the higher porosity found (Table 4) and also the formation of PLA beads.

Porosity is an important parameter when preparing the absorbing material for the X-ray attenuation experiment. As can be seen from Table 4, the porosity of both electrospun n-and m-Bi_2O_3/PLA nanofibre mats was over 70%. This is likely caused by the entangled structure of the randomly-oriented nanofibres, indicating that they were highly porous and thus not ideally suited for X-ray attenuation , especially with the filler $\geq$ 38 wt.%. Further increases to filler loading, beyond 38 wt.%, was not performed due to the decreased density and increased porosity , which is unlikely to give any advantages for future X-ray transmission experiments. The porosity found from the control electrospun PLA nanofibre mat was 88.8%. Thus, if a further investigation was performed for greater

filler loadings the electrospun Bi_2O_3/PLA nanofibre mat would probably have similar or even higher porosity than this controlled sample.

3.2. X-ray attenuations

Fig. 1 shows the XAS linear attenuation coefficient (μ) results of electrospun nanofibre mats for an X-ray energy of 7–20 keV for 0–38 wt% Bi_2O_3 loading. It clearly shows a big difference in μ between electrospun n-Bi_2O_3/PLA nanofibre mats and electrospun m-Bi_2O_3/PLA nanofibre mats at the same filler loadings as the X-ray energy increased. Additionally, Fig. 2 also shows a distinct difference in μ between electrospun n-Bi_2O_3/PLA nanofibre mats and electrospun m-Bi_2O_3/PLA nanofibre mats at the same filler loadings as the X-ray energy increased, which is related to the mammography X-ray effective energy operated at an X-ray tube voltage of 22–49 kV (Fig. 3). These effective energies were determined using half-value layer (HVL) experiments (Suk et al., 2012) on the mammography unit. With kilovoltage X-rays, determination of the HVL of the X-ray beam can be used to characterize the effective energy by converting the measured HVL to the linear attenuation coefficient. The effective energy of a polyenergetic beam is equal to the energy of a monoenergetic X-ray beam that is attenuated at the same rate as the polyenergetic beam which can be determined from tabulated data (Berger et al., 2010).

As can be seen from both Figs. 1 and 2, μ increased with an increase of the filler loading within the PLA matrix for both electrospun n-Bi_2O_3/PLA and m-Bi_2O_3/PLA nanofibre mats, except for the 38 wt% Bi_2O_3 loading where there is a sudden decrease in μ. However, the difference in μ between electrospun n-Bi_2O_3/PLA and m- Bi_2O_3/PLA nanofibre mats becomes higher as the Bi_2O_3 loading increased. These findings support the density and porosity results discussed previously, including the 38 wt% of Bi_2O_3/PLA nanofibre mats which showed low density and high porosity, thus leading to decreased μ. Meanwhile, a comparison of thin films between m-Bi_2O_3/PLA and n-Bi_2O_3/PLA does not totally support the results found from this study for the electrospun Bi_2O_3/PLA nanofibre mats. From Fig. 4, as the X-ray effective energy increased to >17.4 keV (*i.e.* X-ray tube voltages > 35 kV), for the same wt% of Bi_2O_3 filler within this thin film sample, μ for m- Bi_2O_3/PLA thin film and μ by

n- Bi_2O_3/PLA thin film become comparable. They only show significant differences in μ for lower X-ray effective energy, <17.4 keV (*i.e.* X-ray tube voltage 22–35 kV), operated from the mammography unit.

As in our previous study for the comparison of different sizes of WO_3 particles–epoxy composites (Noor Azman et al., 2013), we also obtain similar results for electrospun Bi_2O_3/ PLA nanofibre mats which showed that the attenuation by electrospun n-Bi_2O_3/PLA nanofibre mats is higher than the attenuation by electrospun m-Bi_2O_3/PLA nanofibre mats with the same filler loading in the low-energy regime (22–35 kV operated from the mammography unit). However, by increasing the X-ray tube voltage beyond 35 kV (*i.e.* X-ray effective energy > 17.4 keV), the attenuation by electrospun n-Bi_2O_3/PLA nanofibre mats is still higher than the attenuation by electrospun m-Bi_2O_3/PLA nanofibre mats. In contrast, in our previous work, the differences in the attenuation by micro-sized WO3–epoxy composites and nano-sized WO_3– epoxy composites become indistinguishable when the X-ray tube voltage was increased beyond 35 kV (Noor Azman et al., 2013). Only Bi_2O_3/PLA thin film has a good agreement with our previous results for X-ray tube voltages greater than 35 kV, which shows the indistinguishability in attenuation between m-Bi_2O_3/PLA thin film and n-Bi_2O_3/PLA thin film.

Fig. 5 presents the value of μ for electrospun n-Bi_2O_3/PLA nanofibre mats for all the X-ray beam energies generated by XAS and the mammography unit. The results found from XAS were correlated with those from the mammography unit since the mammography unit produced effective energies of 15–21 keV with the Mo and Rh anode/filter characteristic X-ray energies of 17.5–22.7 keV, while the X-ray energy used with XAS was ~7–20 keV.

In essence, the total X-ray attenuation by the absorbing material is determined by three energy-dissipative mechanisms, namely the photoelectric effect, Compton scattering and pair production. Pair production was not considered in this study because this mechanism will only occur when the photon energy is beyond 611 keV. In the photoelectric absorption process, a photon undergoes an interaction with an absorber atom in which the photon completely disappears. In its place, an energetic photoelectron is ejected from one of the bound shells of the atom. The photoelectric process is the

predominant mode of photon interaction at relatively low photon energies and high atomic number Z, *i.e.* $(Z/E)^3$. Meanwhile, Compton scattering takes place between the incident photon and one of the outer-shell electrons of an atom in the absorbing material. The probability of Compton scattering is almost independent of atomic number Z and X-ray energy E. It is most dominant as the photon energy increases due to a concomitant decrease in the photoelectric effect.

In addition, the number of Bi particles per gram in both n-Bi_2O_3/PLA fibre mats and thin films is higher than their micro-sized counterparts. Hence, the probability of X-rays with lower energies (*i.e.* 7–20 keV and 22–35 kV) interacting and being absorbed by n-Bi_2O_3 filler is higher when compared with their micro-sized counterparts since the photons interact with the absorbing materials mainly by the photoelectric effect.

As a consequence, electrospun n-Bi_2O_3/PLA nanofibre mats are superior to their micro-sized counterparts in terms of X-ray attenuation for all the X-ray beam energies (*i.e.* 7–20 keV and 22–49 kV generated by XAS and mammography, respectively). In contrast, n-Bi_2O_3/PLA thin films are a good X-ray shielding candidate only for the mammography unit at 22–35 kV when compared with m-Bi_2O_3/PLA thin films. Both can be chosen as X-ray shielding materials for voltages greater than 35 kV. The observed similarity in the attenuation results for PLA thin films of n-Bi_2O_3 and m-Bi_2O_3 at the X-ray tube voltage of the mammography unit of more than 35 kV may be attributed to: (a) the decrease of the photoelectric effect, and (b) the domination of the Compton scattering effect when the photon energy increases. The latter effect results in less interaction and absorption of the photons by Bi particles of these thin films; thus the X-ray attenuation of the films is similar. In contrast, electrospun n-Bi_2O_3/PLA nanofibre mats are superior to their micro-sized counterparts in terms of X-ray attenuation at the same energy range. The observed large differences in X-ray attenuation of these fibre mats may be explained by the difference in uniformity of dispersion between nano- and micro-sized Bi particles within the PLA matrix where large agglomerations tend to occur in the latter, thus affecting the final density of the composite.

Hence, the electrospun n-Bi_2O_3/PLA nanofibre mats of all filler loadings (24–38 wt%) are potential candidates in X-ray shielding for all the incident X-ray energies studied either by XAS (7–20 keV) or

mammography (22–49 kV) when compared with their micro-sized counterparts. However, the latter may still be a suitable candidate for X-ray attenuator of scattered radiation which requires lower energy. These electrospun Bi_2O_3/PLA nanofibre mats can be used as a coating material for X-ray shielding because PLA nanofibres provide many benefits such as higher tenacity, resistance to degradation and mechanical properties (Farrington et al., 2005; Haroosh et al., 2012). Besides, since PLA has a higher tenacity, these electrospun Bi_2O_3/PLA nanofibre mats can be fabricated as gloves to be worn by radiation workers when holding radioactive materials or waste (non-clinical use), or used as a liner on examination tables to help attenuate scattered X-rays coming out from patients during medical diagnosis or therapy (using higher X-ray or γ-ray energies in the MeV range) performed by specialist radiographers and radiologists (clinical use).

Meanwhile, n-Bi_2O_3/PLA thin films are good X-ray shielding candidates only for mammography at 25–35 kV, when compared with m-Bi_2O_3/PLA thin films. Both can be chosen as X-ray shielding materials for X-ray tube voltages greater than 35 kV.

3.3. Microstructure analyses

Microstructure analysis of the electrospun nanofibres was performed using both backscattered electrons and secondary electrons to clearly show the difference between the PLA polymer and the embedded Bi elements. Fig. 6(a) shows a SEM image of the control electrospun PLA nanofibres without any Bi_2O_3 filler. The average diameter of these fibres was 854 ± 35 nm. The average diameter of PLA nanofibres increased when 24–34 wt% Bi_2O_3 was added to the PLA solution. For instance, Fig. 6(b) shows the homogeneous nanofibres of 28 wt% n-Bi_2O_3 filler with an average diameter of 971 ± 22 nm. Meanwhile, in Fig. 6(c) the average diameter of 28 wt% m-Bi_2O_3/PLA nanofibres is 911 ± 41 nm with a large variation in fibre diameter and particle agglomerations can be observed.

This indicates that, by increasing the solution viscosity while both the conductivity and the surface tension decreased with the increment of filler (Bi_2O_3) loadings within the PLA solution, the average nanofibre diameter was increased. The significant increase in the viscosity of the solution with increasing filler loadings was due to the increased molecular entanglement which enabled the charged

jet to withstand a larger stretching force (from the Coulombic repulsion) resulting in the coarsening of the nanofibres.

In contrast, a further increase of Bi_2O_3 loading to 38 wt% caused a decrease in the average diameter to 496 ± 32 nm for n-Bi_2O_3/PLA nanofibres which have a maximum diameter of 2.06 ± 0.49 mm and a minimum of 114 ± 2 nm (Fig. 6d). Meanwhile, the average diameter of m-Bi_2O_3/PLA nanofibres is 406 ± 71 nm with a maximum diameter of 1.13 ± 0.23 mm and a minimum of 111 ± 2 nm (Fig. 6e). The unexpected decrease in the average fibre diameter may be attributed to the domination of electrical conductivity when filler loading or viscosity of solution increases. As a result, this leads to the production of fibres with non-uniform diameters, as well as formation of beads and particle agglomerations.

Figs. 7(a)–7(c) illustrate the EDS results for the electrospun n-Bi_2O_3/PLA nanofibre mat with 34 wt% filler loading which confirms the existence of the Bi element from the filler together with elements C and O from the PLA matrix. SEM images of m-Bi_2O_3/PLA and n-Bi_2O_3/PLA thin films with 28 wt% filler loading are shown in Fig. 8, indicating the presence of agglomerations within the PLA matrix.

4. Conclusions

Electrospun nanofibre mats of n-Bi_2O_3/PLA and m-Bi_2O_3/PLA with filler loadings of 24–38 wt% have been successfully fabricated. From the analyses, the electrospun n-Bi_2O_3/PLA nanofibre mats of all filler loadings were found to be superior in attenuating X-rays compared with their micro-sized counterparts because n-Bi_2O_3 may provide more uniform materials since the particle size can affect the microstructure and consequently the density and composition that will then modify the attenuation coefficient of the composite. However, the electrospun Bi_2O_3/PLA nanofibre mats with 38 wt% loading are not recommended for X-ray shielding because of higher porosity compared with the lower filler loadings. The n-Bi_2O_3/PLA thin films are good X-ray shielding candidates only for the mammography unit at 22–35 kV when compared with the m-Bi_2O_3/PLA thin films. The particle size effect on X-ray attenuation diminished as the X-ray tube voltage.

Acknowledgements Part of this research was undertaken on the XAS beamline at the Australian Synchrotron, Victoria, Australia. We thank our colleagues Dr. C. Ng and A/Prof. Z. Sun for assistance with XAS data collection. Also, we would like to thank Carolyn Madeley of Breast Assessment Centre, Royal Perth Hospital, Western Australia for giving us the opportunity to use the mammography unit.

References

An, J.-S., Park, J.-S., Kim, J.-R. & Hong, K. S. (2006). *Journal of the American Ceramic Society* **89**, 3658-3661.

Berger, M. J., Hubbell, J. H., Seltzer, S. M., Chang, J., Coursey, J. S., Sukumar, R., Zucker, D. S. & Olsen, K. (2010).

Botelho, M. Z., Künzel, R., Okuno, E., Levenhagen, R. S., Basegio, T. & Bergmann, C. P. (2011). *Applied Radiation and Isotopes* **69**, 527-530.

Brettmann, B. K., Tsang, S., Forward, K. M., Rutledge, G. C., Myerson, A. S. & Trout, B. L. (2012). *Langmuir* **28**, 9714-9721.

Buyuk, B., Tugrul, A. B., Akarsu, A. C. & Addemir, A. O. (2012). *J. Nano- and Electronic Physics* **4**, 01010(01011)-01010(01014).

Chanthima, N., Kaekwkhao, J., Kedkaew, C., Chewpraditkul, W., Pokaipisit, A. & Limsuwan, P. (2011). *Progress in Nuclear Sicence and Technology* **1**, 106-109.

Demir, M. M., Gulgun, M. A., Menceloglu, Y. Z., Erman, B., Abramchuk, S. S., Makhaeva, E. E., Khokhlov, A. R., Matveeva, V. G. & Sulman, M. G. (2004). *Macromolecules* **37**, 1787-1792.

El Haber, F. & Froyer, G. (2008). *Journal of the University of Chemical Technology and Metallurgy* **43**, 283-290.

Faccini, M., Vaquero, C. & Amantia, D. (2012). *J. Nanomaterials* **2012**, 1-9.

Farrington, D. W., Lunt, J., Davies, S. & Blackburn, R. S. (2005). *Poly (lactic acid) fibers*, pp. 191-220. Cambridge, United Kingdom: Woodhead Publishing Series in Textiles.

Granmayeh Rad, A., Abbasi, H. & Afzali, M. H. (2011). *Physics Procedia* **22**, 203-208.

Haiwen, X., Kai-Zhong, G., Yiming, S. & Song, X. (2006). *Journal of Physics D: Applied Physics* **39**, 4746.

Haroosh, H. J., Chaudhary, D. S. & Dong, Y. (2012). *Journal of Applied Polymer Science* **124**, 3930-3939.

Hu, W., Huang, Z. M. & Liu, X. Y. (2010). *Nanotechnology* **21**, 315104.

Huang, S., Kang, X., Cheng, Z., Ma, P., Jia, Y. & Lin, J. (2012). *J Colloid Interface Sci* **387**, 285-291.

Huang, X. & El-Sayed, M. A. (2010). *Journal of Advanced Research* **1**, 13-28.

Künzel, R. & Okuno, E. (2012). *Applied Radiation and Isotopes* **70**, 781-784.

Lee, S. & Obendorf, S. K. (2007). *Textile Research Journal* **77**, 696-702.

M.G, L. (2008). *Journal of Alloys and Compounds* **449**, 242-245.

Molamma, P. P., Venugopal, J., Casey, K. C. & Ramakrishna, S. (2008). *Nanotechnology* **19**, 455102.

Noor Azman, N. Z., Siddiqui, S. A., Hart, R. & Low, I. M. (2013). *Applied Radiation and Isotopes* **71**, 62-67.

Patra, C. R., Bhattacharya, R., Mukhopadhyay, D. & Mukherjee, P. (2010). *Advanced Drug Delivery Reviews* **62**, 346-361.

Popov, A. (2009). *SPIE Newsroom* **24**, 1-2.

Rajeswari, R., Jayarama Reddy, V., Subramanian, S., Shayanti, M., Radhakrishnan, S. & Seeram, R. (2012). *Nanotechnology* **23**, 385102.

Robert, R. D. (2005).

Russo, G. & Lamberti, G. (2011). *Journal of Applied Polymer Science* **122**, 3551-3556.
Sahare, P. D., Ranju, R., Numan, S. & Lochab, S. P. (2007). *Journal of Physics D: Applied Physics* **40**, 759.
Shanshan, B., Jayaram, S. H. & Cherney, E. A. (2010). *Electrical Insulation and Dielectric Phenomena (CEIDP), 2010 Annual Report Conference on*, pp. 1-4.
Sill, T. J. & von Recum, H. A. (2008). *Biomaterials* **29**, 1989-2006.
Storrie, H. & Mooney, D. J. (2006). *Advanced Drug Delivery Reviews* **58**, 500-514.
Suk, C. C., Wei, L. J. & Harun, A. Z. (2012). *Malays J Med Sci.* **19**, 22-28.
Yiin-Kuen, F. & Li-Chih, L. (2013). *Nanotechnology* **24**, 055301.
Yu, D. G., Shen, X. X., Chris, B. W., Kenneth, W., Zhu, L. M. & Bligh, S. W. A. (2009). *Nanotechnology* **20**, 055104.

Table 1 Prepared electrospun nanofibre mats with different weight fractions of filler (Bi_2O_3) and PLA.

Electrospun Bi_2O_3 PLA nanofibre mat by weight fraction (wt%)	
Filler (Bi_2O_3)	PLA
24	76
28	72
34	66
38	62

Table 2 Anode/filter combination operated by the mammography machine.

X-ray tube voltage (kV)	Anode/filter combination
22 25 30	Mo/Mo[a]
35 40	Mo/Rh[b]
45 49	Rh/Rh[c]

[a] Molybdenum anode/molybdenum filter.

[b] Molybdenum anode/rhodium filter.

[c] Rhodium anode/rhodium filter.

Table 3 Density of electrospun Bi_2O_3/PLA nanofibre mats and Bi_2O_3/PLA thin films.

Filler (Bi_2O_3) weight fraction (wt%)	Density (cm^3/g)				
	Theoretical	Electrospun nanofibre mat		Thin films	
		nano	micro	nano	micro
24	1.56	0.27	0.25	1.54	1.50
28	1.63	0.40	0.37	1.59	1.52
34	1.75	0.49	0.45	1.69	1.64
38	1.84	0.30	0.24	1.77	1.72

Table 4 Porosity of electrospun Bi_2O_3/PLA nanofibre mats.

Filler (Bi_2O_3) weight fraction (wt%)	Porosity (%)	
	Nano-Bi_2O_3/PLA nanofibre mat	Micro-Bi_2O_3/PLA nanofibre mat
0	88.8	88.8
24	83.0	84.0
28	75.4	77.0
34	72.1	74.3
38	83.6	87.0

Figure 1 Linear attenuation coefficient as a function of synchrotron radiation energy operated by XAS (7 – 20 keV) for all Bi_2O_3 loading (0 – 38 wt.%) of the electrospun n-Bi_2O_3/PLA and m-Bi_2O_3/PLA nanofibre mats.

Figure 2 Linear attenuation coefficient as a function of effective energy operated by various X-ray tube voltages of the mammography unit (22-49 kV) for all Bi_2O_3 loading (0 – 38 wt.%) of the electrospun n-Bi_2O_3/PLA and m-Bi_2O_3/PLA nanofibre mats.

Figure 3 Effective energy as a function of the X-ray tube voltages operated by mammography unit determined from half value layer measurements.

Figure 4 Linear attenuation coefficient as a function of the effective energy operated by various X-ray tube voltages of the mammography unit (22-49 kV) for all Bi_2O_3 loading (0 – 38 wt.%) of the n-Bi_2O_3/PLA and m-Bi_2O_3/PLA thin films.

Figure 5 Comparison of linear attenuation coefficient for the electrospun n-Bi_2O_3/PLA nanofibre mats for all the X-ray beam energy generated by XAS unit and mammography unit.

Figure 6 SEM images using for each figure, the backscattered electron technique (left) and the secondary electron technique (right) for (a) the control electrospun PLA nanofibres without any particles (0 wt% of Bi_2O_3); (b) 28 wt% Bi_2O_3 of electrospun n- Bi_2O_3/PLA nanofibres; (c) 28 wt% Bi_2O_3 of electrospun m-Bi_2O_3/PLA nanofibres; (d) 38 wt% Bi_2O_3 of electrospun n-Bi_2O_3/PLA nanofibres; and (e) 38 wt% Bi_2O_3 of electrospun m-Bi_2O_3/PLA nanofibres.

Figure 7 (a) SEM image used for EDS analyses on 34 wt% Bi_2O_3 of the electrospun n-Bi_2O_3/PLA nanofibres to prove that only Bi particles are detected other than C and O which is the composition of PLA; EDS analyses for (b) point 1 and; (c) point 2 marked in (a).

Figure 8 SEM images of a thin film of 28 wt% Bi_2O_3 for m-Bi_2O_3/PLA on the left (clear agglomerations can be seen) and n-Bi_2O_3/PLA on the right.

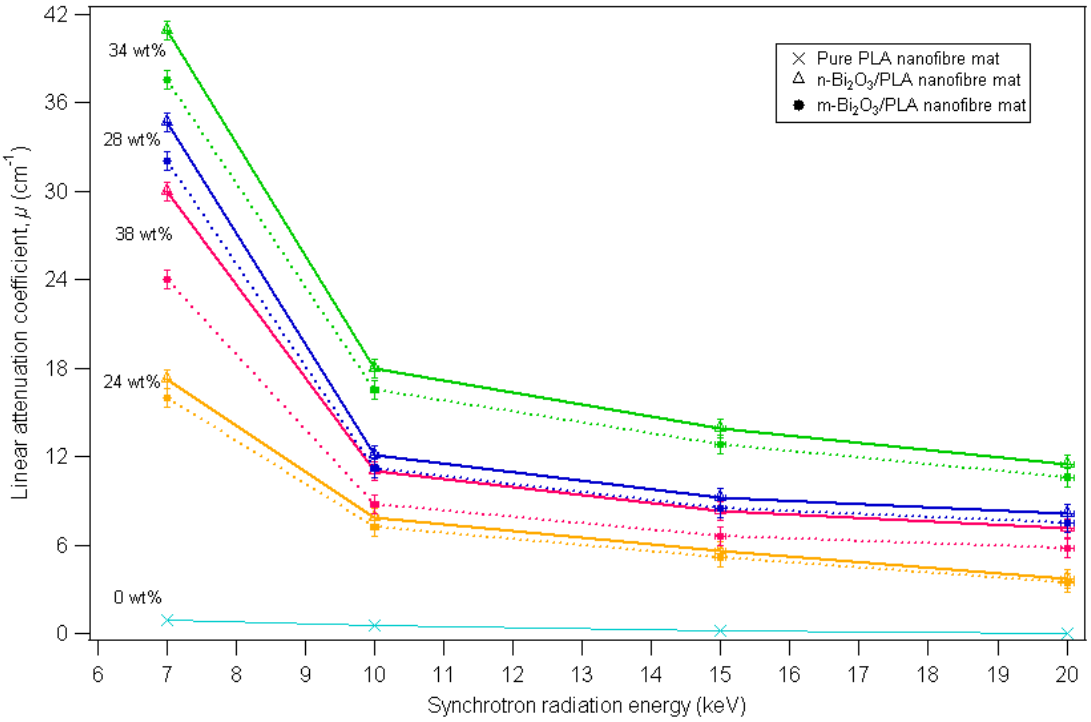
Linear attenuation coefficient, μ (cm^{-1})
Synchrotron radiation energy (keV)
Pure PLA nanofibre mat
n-Bi_2O_3/PLA nanofibre mat
m-Bi_2O_3/PLA nanofibre mat
34 wt%
28 wt%
38 wt%
24 wt%
0 wt%
0
6
12
18
24
30
36
42
6
7
8
9
10
11
12
13
14
15
16
17
18
19
20

Figure 1

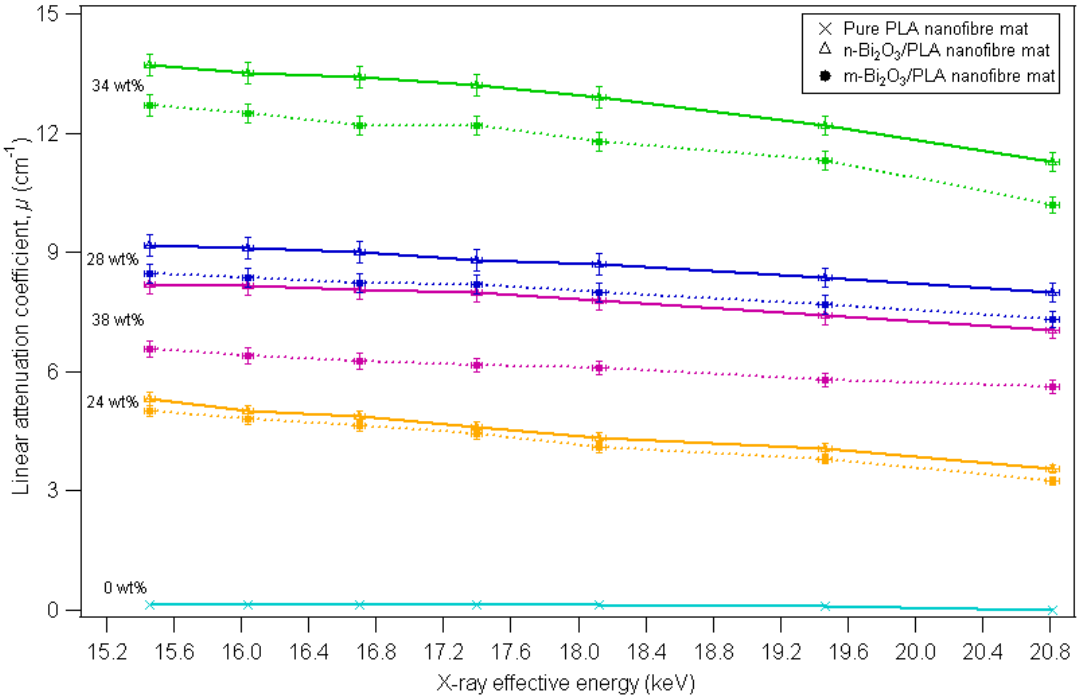
Pure PLA nanofibre mat
n-Bi2O3/PLA nanofibre mat
m-Bi2O3/PLA nanofibre mat
34 wt%
28 wt%
38 wt%
24 wt%
0 wt%
Linear attenuation coefficient, μ (cm-1)
X-ray effective energy (keV)
0
3
6
9
12
15
15.2
15.6
16.0
16.4
16.8
17.2
17.6
18.0
18.4
18.8
19.2
19.6
20.0
20.4
20.8

Figure 2

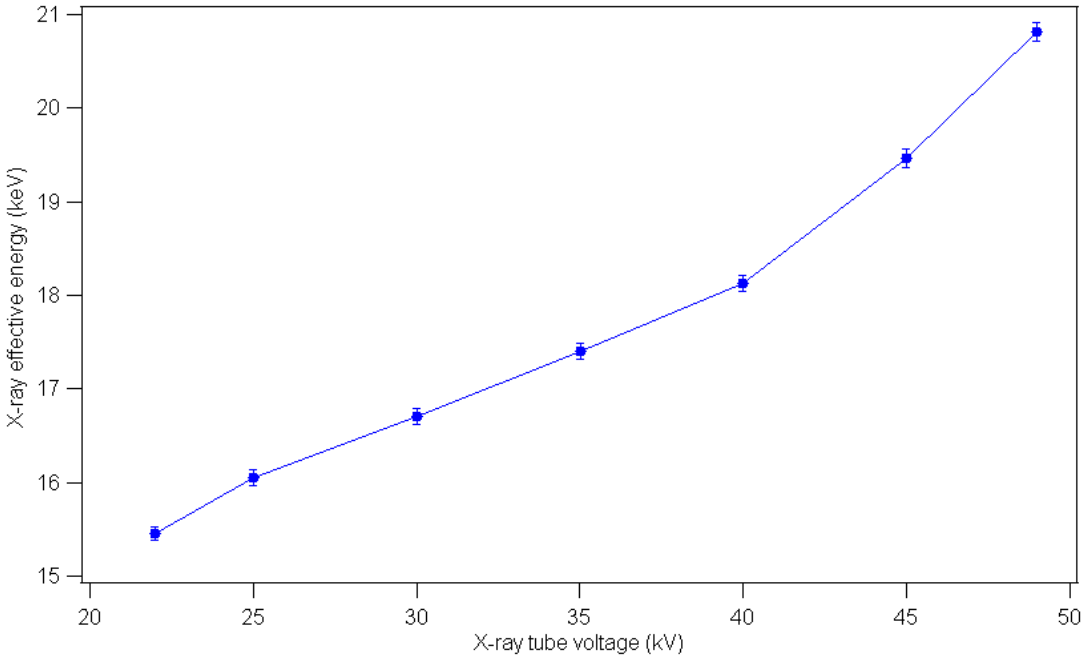
21
20
19
18
17
16
15
X-ray effective energy (keV)
20
25
30
35
40
45
50
X-ray tube voltage (kV)

Figure 3

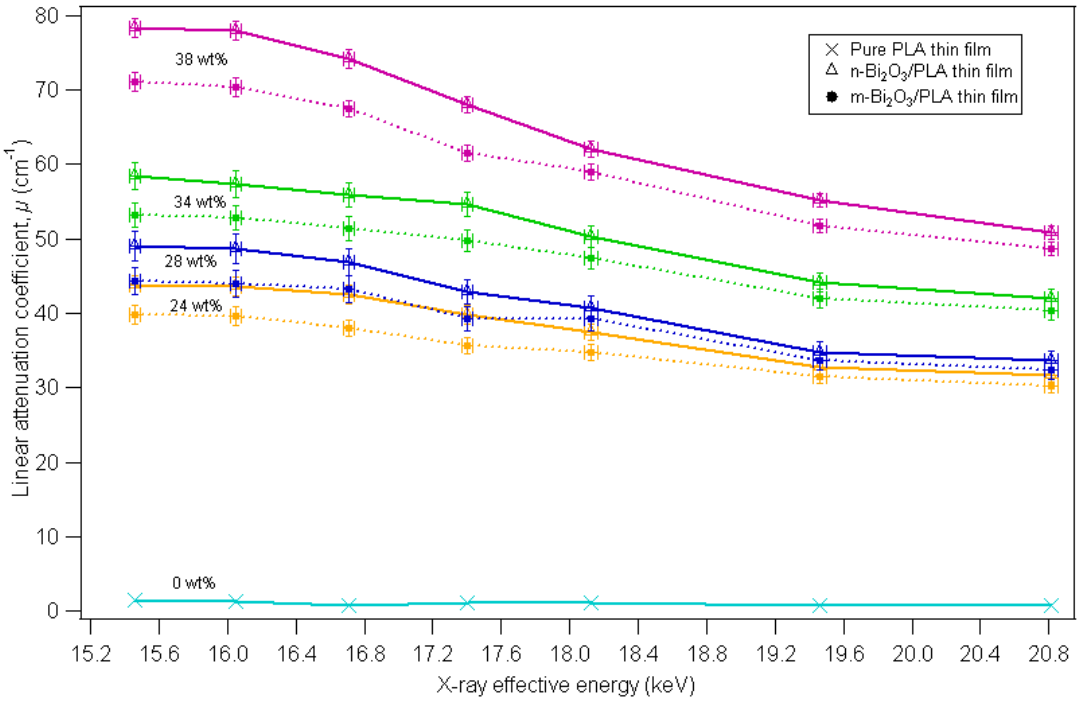
Pure PLA thin film
n-Bi2O3/PLA thin film
m-Bi2O3/PLA thin film
38 wt%
34 wt%
28 wt%
24 wt%
0 wt%
Linear attenuation coefficient, μ (cm-1)
X-ray effective energy (keV)
80
70
60
50
40
30
20
10
0
15.2
15.6
16.0
16.4
16.8
17.2
17.6
18.0
18.4
18.8
19.2
19.6
20.0
20.4
20.8

Figure 4

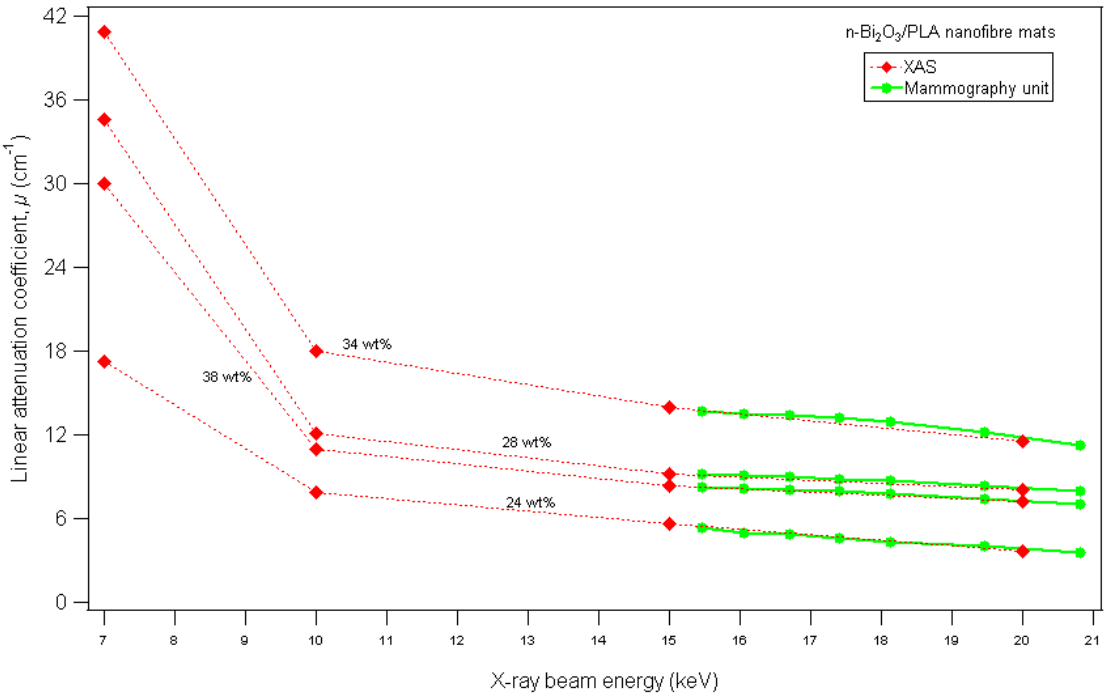
n-Bi2O3/PLA nanofibre mats
XAS
Mammography unit
Linear attenuation coefficient, μ (cm-1)
X-ray beam energy (keV)
34 wt%
38 wt%
28 wt%
24 wt%
0
6
12
18
24
30
36
42
7
8
9
10
11
12
13
14
15
16
17
18
19
20
21

Figure 5

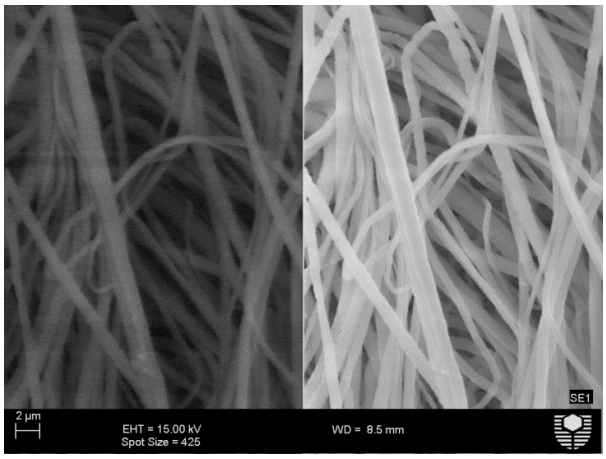

(a)

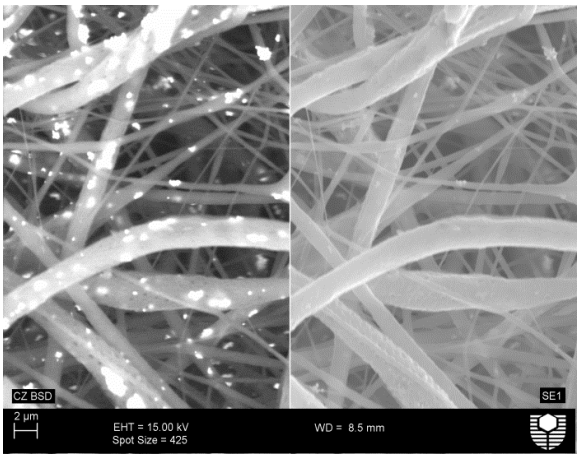

(d)

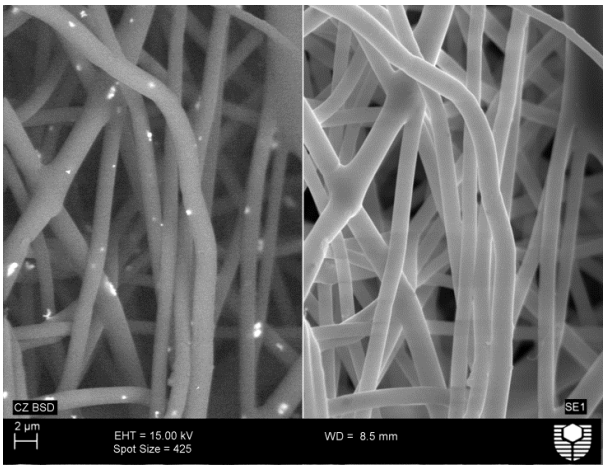

(b)

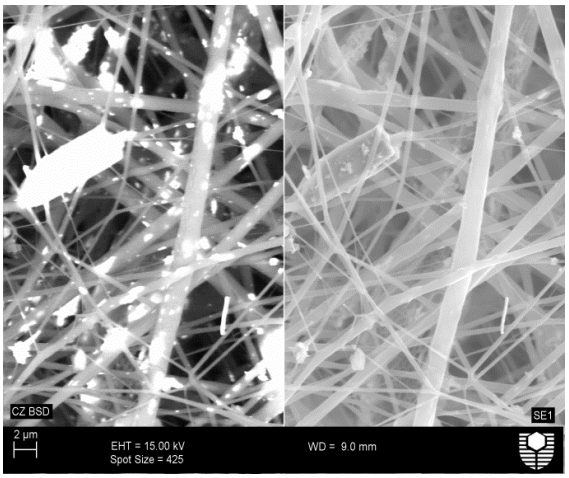

(e)

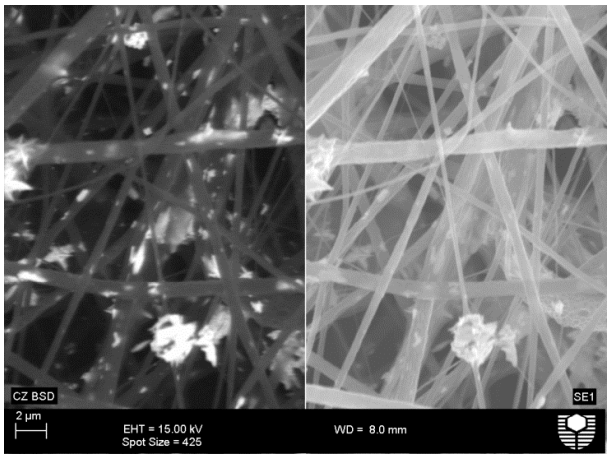

(c)

Figure 6

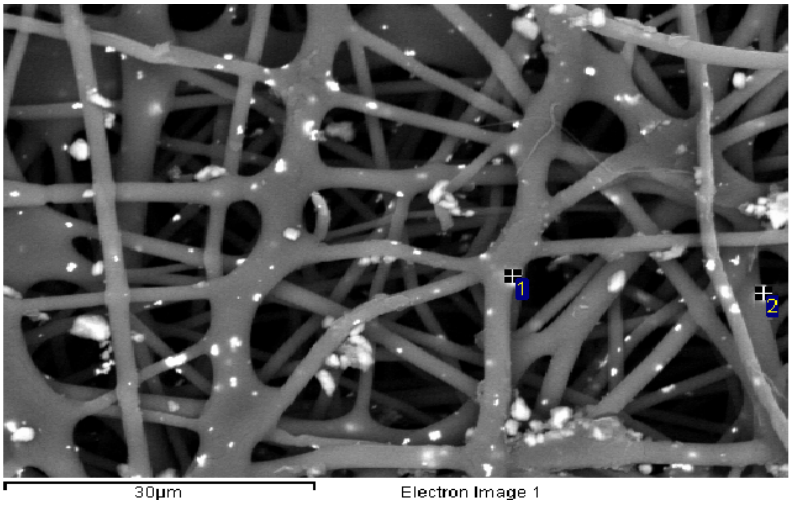
1
2
30µm
Electron Image 1

(a)

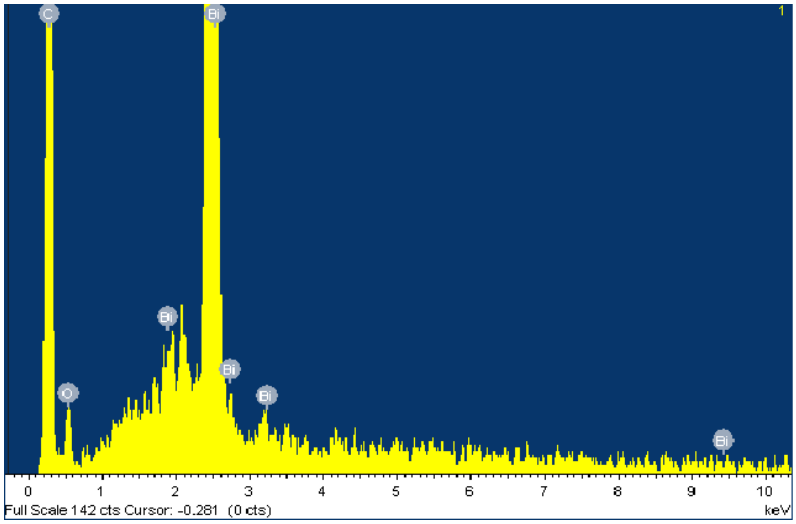
C
Bi
Bi
O
Bi
Bi
Bi
1
0 1 2 3 4 5 6 7 8 9 10
Full Scale 142 cts Cursor: -0.281 (0 cts)
keV

(b)

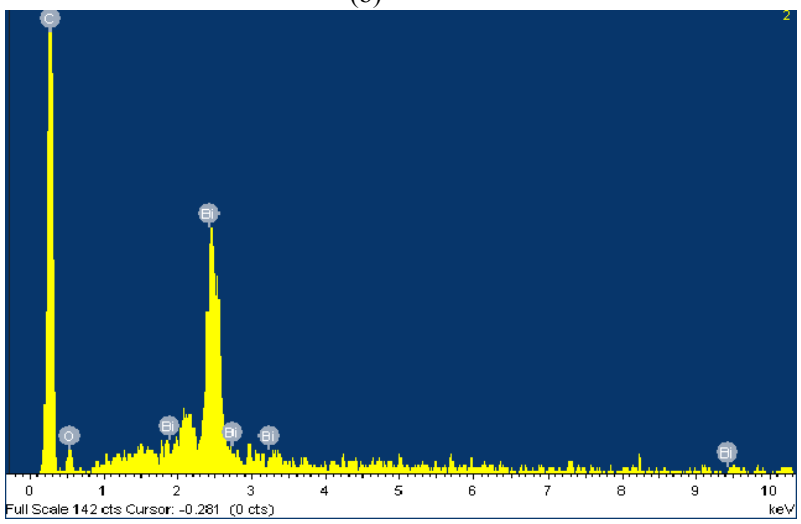
C
Bi
O
Bi
Bi
Bi
Bi
2
0 1 2 3 4 5 6 7 8 9 10
Full Scale 142 cts Cursor: -0.281 (0 cts)
keV

(c)

Figure 7

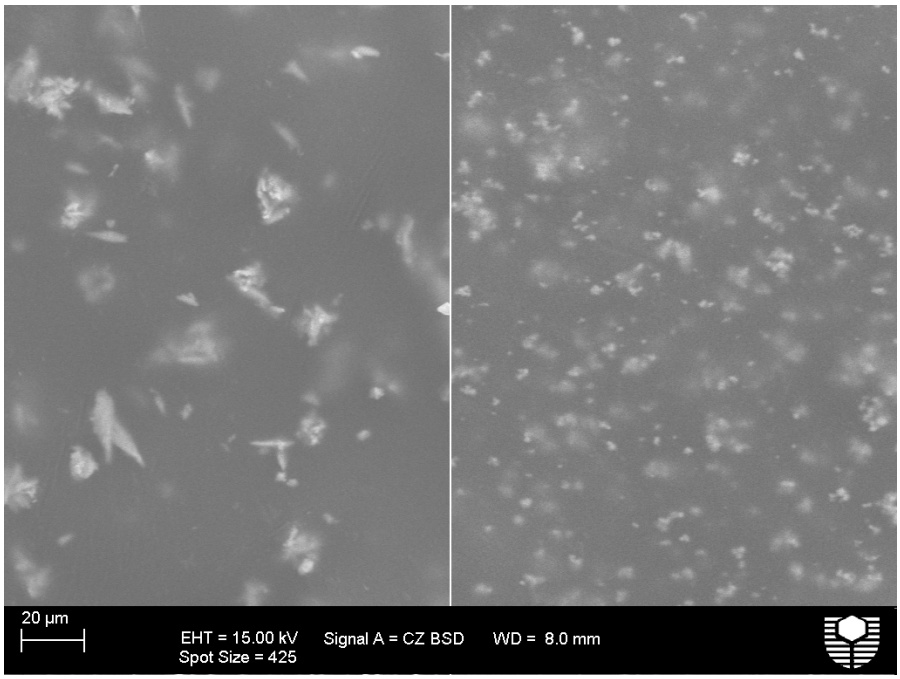

Figure 8